JOURNAL OF PROPULSION AND POWER
Vol. 12, No. 3, May–June 1996

Impact Characteristics of Hailstones Simulating Ingestion by Turbofan Aeroengines

H. Pan* and P. M. Render†
Loughborough University of Technology, Loughborough, Leicestershire LE11 3TU, England, United Kingdom

To study hail ingestion of turbofan engines, it is essential to have an understanding about the impact of hailstones upon a solid surface. Basic ice impact characteristics in terms of postimpact particle size, velocity, and mass distribution were studied experimentally with simulated hailstones. Two techniques were used, i.e., patternator and still photography. The advantages and disadvantages of each technique are discussed and the results from each technique presented. A parametric study was carried out, and the parameters investigated included impact angle, approach speed, and initial size of the simulated hailstones. Based on the experimental results, a set of empirical rules is defined for the basic disintegration characteristics of simulated hailstones upon impact.

Nomenclature

a_L = speed of sound in the laboratory, assumed constant at 340 m/s
D_0 = initial ice ball size, mm
d = postimpact particle size, mm
d_{max} = maximum particle size, mm
d_{mean} = mean particle size, mm
k_δ = ratio δ/d
N_d = Rosin–Rammler coefficient for size distribution
N_v = Rosin–Rammler coefficient for velocity distribution
r = radial coordinate with the origin at impact point, m
t = time from the impact to image taken, s
V_0 = impact velocity, m/s
v = postimpact particle velocity, m/s
v_{max} = maximum postimpact particle velocity, m/s
v_{mean} = mean postimpact particle velocity, m/s
β = direction of ice particle travel after impact, deg
Δt = time interval between two photographic flashes, s
δ = particle depth, mm
θ = incidence angle between the ice ball path and the plate, deg
μ_d = mass fraction for size distribution of particles after impact
μ_v = mass fraction for velocity distribution of particles after impact

Introduction

RAIN, snow, and hail are known to have serious effects on turbofan engines. Hail is a rare phenomenon in nature for most places in the world, but it is more hazardous compared to rain and snow because of its solid characteristic and high concentration of water. Several instances during commercial flights have reported engine power loss during hailstorms. It is presently being considered by airworthiness authorities whether to add certification procedures concerning hail ingestion, and an understanding of hail ingestion mechanisms in turbofan engines is now required. The research work is concentrated on aircraft descent when the engine power setting is low and the engine has the lowest tolerance against hail.

The mechanism by which ice deteriorates the engine performance can be qualitatively illustrated by following the route of the ingested ice within the engine. At the inlet stage, the hailstones may hit the nacelle, spinner, or fan blades. Ice content in the air can increase the load on the fan shaft, which affects the engine performance. After passing the fan, ice will be flying downstream and is subject to aerodynamic drag. It is believed that much of the ice remains in a solid state as it passes through the fan stage because of the low temperature and short passage time. When the ice reaches the splitter, part of the ice goes into the core and the rest goes into the bypass duct. The ice that goes into the bypass duct does no harm to the engine, but the ice that enters the core will pass into the stages of the high-pressure compressor. Here it melts, forming liquid water or even vapor, and eventually enters the combustion chamber. Water, whether in the form of ice, liquid, or vapor, changes the temperature and density of air, which consequently changes the air pressure and velocity distribution in the compressor blade channels, and alters the pressure acting on the blades. This can result in the operating condition imposed upon the compressor blades departing too far from the design working condition, which in turn causes compressor stall or surge to occur. When water enters the combustion chamber, it can cause an increased fuel demand that can induce flame-out.

It is reasonable to assume that surge margins and flame-out characteristics are related to the quantity, size, and velocities of ice particles entering an engine. However, no studies have been found that quantify the deterioration of engine performance with ice particle parameters. Numerical models may in the future allow such studies to be carried out, and one such model is currently being developed to track ice particle movements within an engine.[1] A computational fluid dynamics calculation is carried out for the engine geometry without the hailstones in the flow. This calculation yields the flowfield of the inlet and fan stage. Hailstones are then seeded into the flowfield, assuming that they do not affect the flow. The ice particles fly towards the engine inlet while being subjected to aerodynamic drag. By selecting the proper drag coefficient, the movements of the hailstones are predicted and tracked when they are airborne. Once a hailstone hits a solid surface, problems arise because of the lack of knowledge about ice particle impacts. It can be assumed that the impact will shatter the hailstones in most cases, but impact characteristics in terms of

Presented as Paper 94-2956 at the AIAA/ASME/SAE/ASEE 30th Joint Propulsion Conference and Exhibit, Indianapolis, IN, June 27–29, 1994; received April 14, 1995; revision received Oct. 16, 1995; accepted for publication Nov. 26, 1995.

*Research Assistant, Department of Aeronautical and Automotive Engineering and Transport Studies.
†Lecturer, Department of Aeronautical and Automotive Engineering and Transport Studies. Member AIAA.

postimpact particle size, postimpact particle velocity, and postimpact direction of travel are unknown. This information is critical because for any further tracking, the postimpact particle size will determine the drag, the postimpact velocity will decide the initial momentum, and the postimpact direction of travel will decide the orientation. The experimental work described in this article was devoted to obtaining these basic ice impact characteristics.

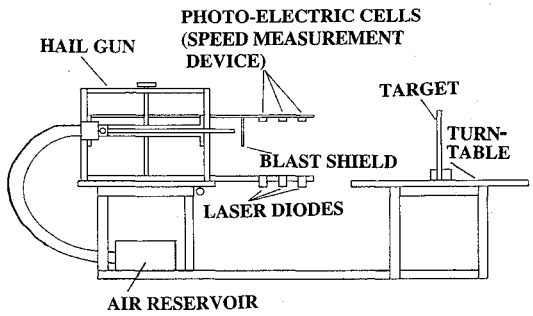

Fig. 1 Test rig.

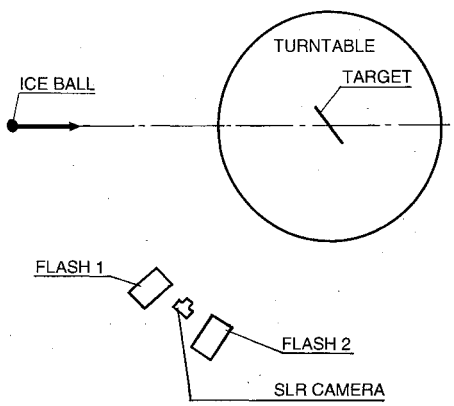

Fig. 2 Arrangement of camera and flash units.

Reference 2 describes a numerical model, but the ice impact characteristics employed were lacking in experimental support. Experimental work has been carried out on water impingement[3,4] and sand impacts,[5-7] but no literature was found about ice particle impacts. Although the experimental techniques used in the study of water and sand impacts may be of relevance to hail impacts, the results are not applicable because of differences in the physical properties of water, sand, and ice.

Test Rig and Experimental Techniques

A detailed description of the test rig is given in Ref. 1. Figure 1 is a sketch of the rig. A hail gun operated by compressed air was built. The gun could fire 12.7-mm-diam simulated hailstones at speeds up to 190 m/s. Simulated hailstones were made from flaked ice molded into 12.7-mm-spherical shapes and left in a freezer at −40°C for 24 h. In this article, the term ice ball or simply ice is used to refer to the simulated hailstones, while hail or hailstone is only used for naturally formed hail. The speed of the ice balls was monitored with three laser beams placed in front of the gun barrel. The distance between the lasers was known. Each photoelectric cell gave a pulse when the laser beam was cut by an ice ball. The pulses were fed into a computer timer so that the time interval between them could be measured. Knowing the distances between the lasers and the time intervals, the ice ball speed was calculated. The three laser-diodes were also used to detect ice ball breakup. A broken ice ball gave more than three pulses when cutting the laser beams. When a broken ice ball occurred, the shot was taken as suspect and ignored.

During the research, two techniques were used to study basic ice ball impact characteristics: 1) patternator and 2) still photography. Each technique has its advantages and disadvantages, but they can complement each other and provide clear views of various aspects of ice impact characteristics. An introduction and comparison of the two techniques is given next.

The patternator consisted of a matrix of metal tubes filled with absorbent tissue.[1] The patternator elements collected the ice particles resulting from the ice ball impact, and the tissue

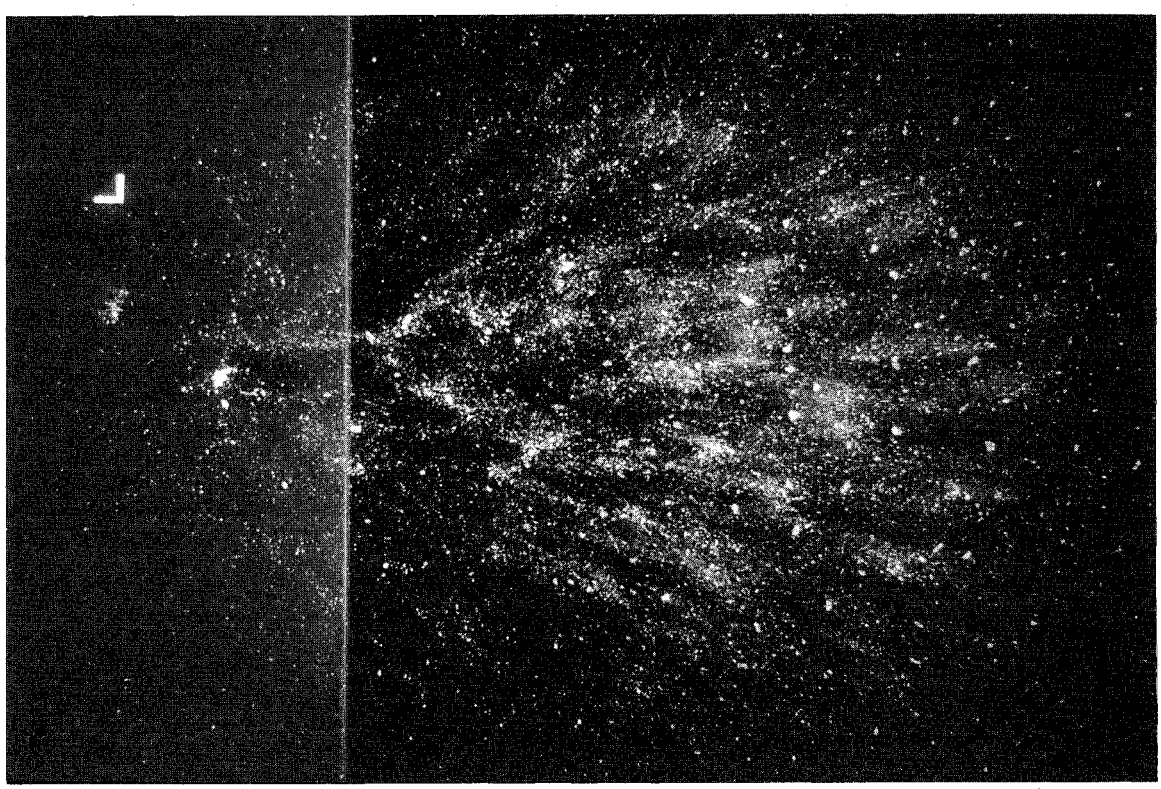

Fig. 3 Photograph using a single flash unit. Test case 3: V_0 = 175 m/s, θ = 45 deg, and D_0 = 12.7 mm.

held the water from any melted ice. By weighing the elements before and after the tests, the amount of ice and water captured in each element was obtained and the mass distribution found. The patternator technique is cheap and easy to run, and so a large number of tests can be done to give a high level of confidence. The disadvantage of the patternator is that it gives no information about postimpact particle size and velocity.

The still photography technique employed a conventional single lens reflex (SLR) camera and one or two high-speed (short-duration) flash guns. The arrangement is sketched in Fig. 2. The flash guns generated 1-μs duration flashes. These very short flashes froze the movement of the ice particles. The test was conducted in darkness with the camera shutter initially left open, and then shut after the flash guns were fired. If one flash gun was used, each ice particle left one image on the photograph. Particle sizes were measured from the photographs and mass distribution obtained. If two flash units were used with a known time interval between them, each particle left two images on the photograph, hence, the velocities of the particles could be determined. Figure 3 is one of the single-flash photographs and Fig. 4 is one of the double-flash photographs (case 3 in Table 1). In Fig. 4, the time interval between the two flashes was 39.7 μs. Both photographs are for an ice ball impact on a flat steel plate. The size of the plate was 200 mm wide by 350 mm high. In Figs. 3 and 4 the L-shaped mark on the plate is a length reference showing 10 mm vertically and 10 mm horizontally. The ice ball hit the plate that is on the left of the photograph, with the ice particles traveling from left to right. The photographs were taken approximately 1.8 ms after the impact. The disadvantage of still photography is that it can only give one photograph of a given impact. Therefore, changes in mass distribution and particle velocity with time, after an impact, cannot be readily determined.

Table 1 Test cases

Case no.	Ice ball diameter, mm	Incidence angle, deg	Impact velocity, m/s	No. of runs
1	12.7	20	175	3
2	12.7	30	175	3
3	12.7	45	175	3
4	12.7	60	175	3
5	12.7	45	102	3
6	12.7	45	136	3
7	19.0	45	136	3

Test Cases

A matrix of test cases was carried out using the still photography technique (Table 1). These test cases were for the flat plate and covered a range of incidence angles, impact velocities, and ice ball sizes. For each case, three runs were carried out to ensure repeatability.

Experimental Results

Postimpact Particle Size

The postimpact particle sizes were obtained from the photographs employing a single flash (Fig. 3). An effort was made to set up an automatic system to measure the particle sizes. This failed because the photographs contained a wide variation of gray level, and also some particles overlapped each other. When image-processing systems were used to analyze the photographs, some particles were wiped out or reduced in size because their images contained a gray level that fell below the cutoff threshold of the image processor. Where the particles overlapped, they were joined together to form one particle. No automatic image processing facility was found to give an acceptable interpretation of the photographs. Therefore, the analysis of the photographs was done by manual measurement. The photographic slide was projected onto a screen with a grid to cut the interrogation area into small segments. The particle size measurement was done using a template with various sizes of holes ranging from 1 to 14 mm, in steps of 0.5 mm. As the projected image was at least twice the full size, particles were sized to a resolution higher than 0.25 mm.

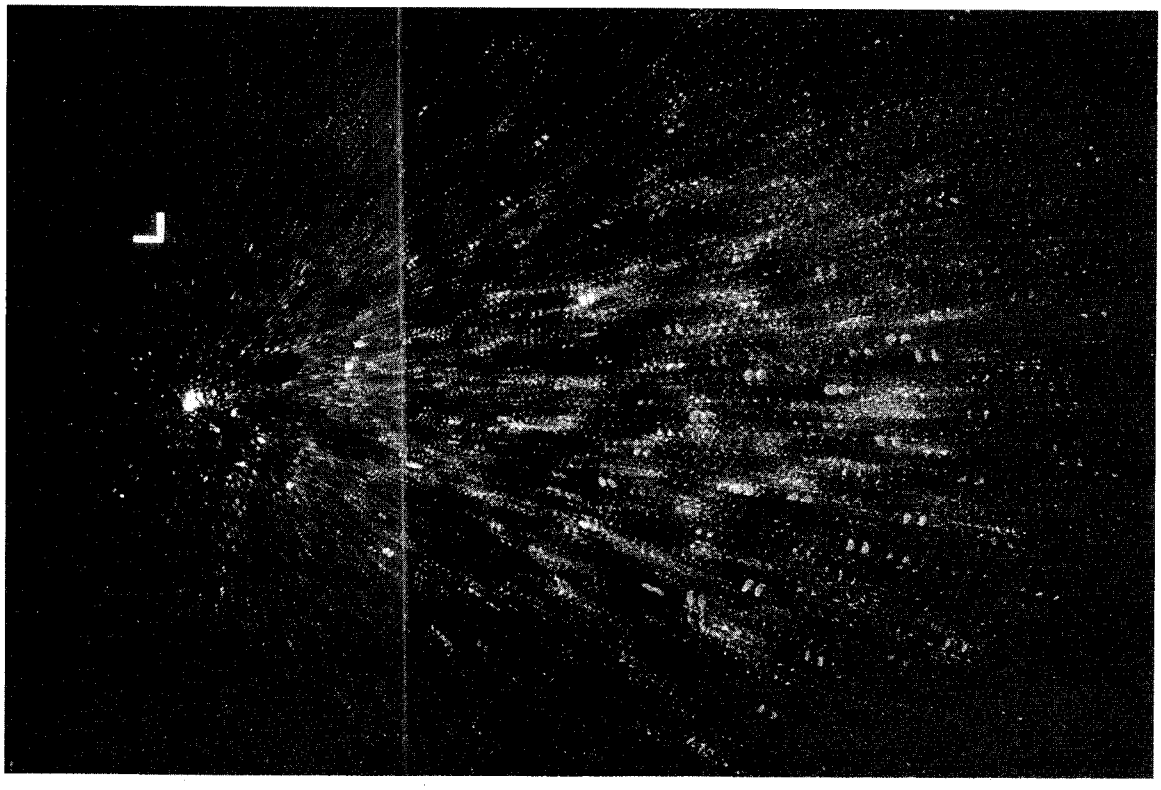

Fig. 4 Photograph using two flash units. Test case 3: V_0 = 175 m/s, θ = 45 deg, and D_0 = 12.7 mm.

Particle sizes were analyzed against mass fraction, as shown in Fig. 5. Mass fraction for a certain size is defined as the ratio of the mass of the particles whose size is equal to or less than this certain size divided by the total mass of particles seen in the photograph. The commonly used Rosin–Rammler[8] distribution was found to give a good fit of the experimental data, and is shown as a solid line, denoted by R–R distribution, in Fig. 5. The expression of Rosin–Rammler distribution can be written as

$$\mu_d = 1 - \exp[-(d/d_{\text{mean}})^{N_d}] \tag{1}$$

in which d_{mean} is the mean particle size defined as the size greater or equal to 63% of the ice particles. The Rosin–Rammler coefficient N_d can be varied to produce a suitable curve through the experimental data. The values of $d_{\max}$, d_{mean}, and N_d have been shown to depend upon the impact velocity and angle. Therefore, when defining any impact rules, the squared normal velocity $(V_0 \sin \theta)^2$ was assumed to be a primary variable. As a first approximation, this seems reasonable, since particle size would be expected to be a function of normal impact energy. The coefficient N_d did not appear to be related to $(V_0 \sin \theta)^2$, and was assumed to be simply a function of $(V_0 \sin \theta)$. A set of empirical rules was obtained by curve-fitting the experimental data using the rule of least squares, and the resulting curves are shown in Figs. 6–8. The corresponding expressions for these curves are

$$d_{\max}/D_0 = 0.437 - 0.922(V_0 \sin \theta/a_L)^2 \tag{2}$$

$$d_{\text{mean}}/D_0 = 0.3 - (V_0 \sin \theta/a_L)^2 \tag{3}$$

$$N_d = 3.512 - 4(V_0 \sin \theta/a_L) \tag{4}$$

The previous equations are simple regressions from experimental results, and should only be applied to the range of $(V_0 \sin \theta/a_L)$ covered by the experimental data. The quantity a_L was used simply for the purpose of nondimensionalization and curve fitting. It should be treated as a constant given by a_L = 340 m/s.

Some assumptions used during the analysis need to be pointed out.

1) Ice balls were weighed before firing. There was a loss of mass in the gun barrel and while the ice ball was moving through the air towards the target. From the patternator results, 85% of the ice was caught on average in the patternator after impact. Therefore, it was assumed that the ice seen in the photographs (Fig. 3) was 85% of the mass of ice fired.

2) In Fig. 3, only the two-dimensional view can be seen. No measurement could be made for the third dimension, and so the mass calculation had to be done on the basis of some

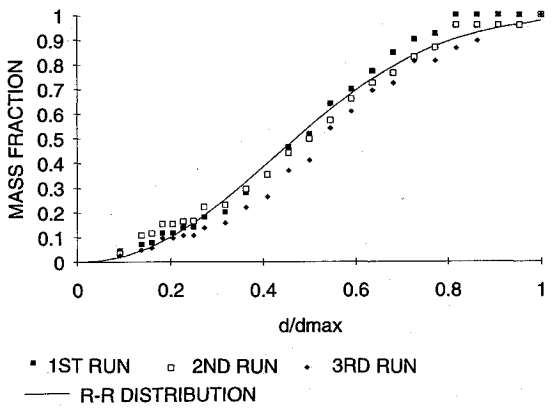

Fig. 5 Postimpact particle size distribution, test case 3; Rosin–Rammler parameters: $d_{\max}$ = 3.85 mm, d_{mean} = 2.38 mm, and N_d = 2.33.

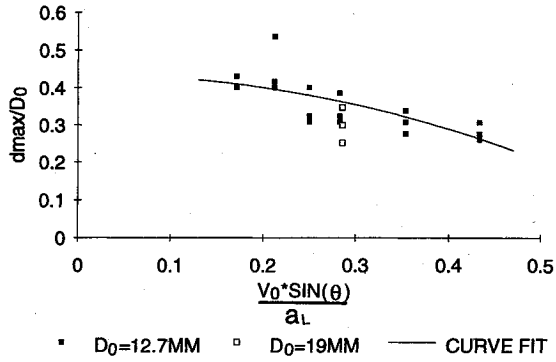

Fig. 6 Curve fit for $d_{\max}$.

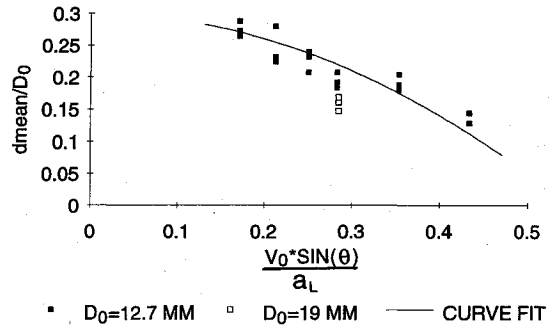

Fig. 7 Curve fit for d_{mean}.

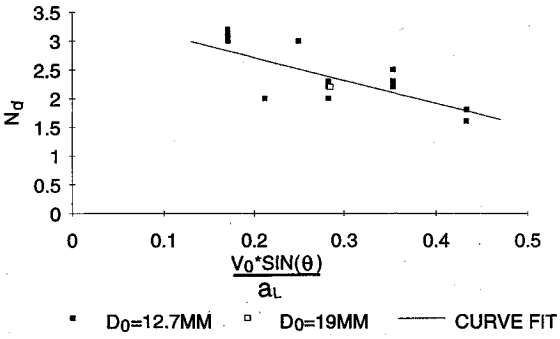

Fig. 8 Curve fit for N_d.

assumptions about the third dimension. It was reasonable to assume that after the impact, the ice particles were flakes rather than spheres, and that most of the flakes were flying in a flat manner along the surface of the plate. Furthermore, it was assumed that for every particle, there was a constant ratio between its depth δ, i.e., the third dimension, and its diameter d. This assumption could be expressed as

$$k_\delta = \delta/d = \text{const} \tag{5}$$

where k_δ could be obtained from mass conservation. As stated, the ice seen on the photograph was 85% of the original ice ball fired, hence,

$$\frac{1}{6}\pi D_0^3 \cdot 0.85 = \sum \frac{1}{4}\pi d^2 k_\delta \cdot d \tag{6}$$

From this equation, the average value of k_δ obtained was 0.65.

Postimpact Mass Distribution

Experiments with the patternator have shown that after an impact, ice particles do not bounce. In other words, ice particles lose their normal velocity and fly in a narrow band along the surface of the plate.[1] This reduces the mass distribution problem to the study of the mass in the plane of the plate

surface. A radial coordinate system (r, β) was set up where r was the radial distance from the impact point. The direction of travel of the ice particles β was measured in degrees from a horizontal axis through the impact point. The main concern was to determine the mass of ice against the direction of travel. These data were obtained from single-image photographs (Fig. 3). Using the previously described grid, the mass of particles in each segment was readily obtained since the size of all the particles in each segment had been previously determined when deriving Fig. 5. Knowing the depth δ of each particle [Eqs. (5) and (6)], the mass of ice in each segment could be determined. If the mass of ice in each of the segments along the same angular position is added up, then the result is the amount of ice traveling in a given direction β. The result is presented in normalized form, as shown in Fig. 9. The horizontal axis is the direction of travel β and the vertical axis is the percentage of ice per degree of angle, i.e.,

$$\frac{\text{mass of ice in segments along the same angular position}}{\text{total mass of ice in photograph} \times \text{angle of segments}}$$

To obtain the amount of ice between any two values of β, one needs to integrate the curve between the two angles. The three lines are results from three different shots of identical conditions (case 3). There are similarities between the figures, but also considerable differences. This is understandable because no two ice balls break up in exactly the same way. The large pieces of ice dominate the mass distribution, and produce spikes and dips in the distribution curve. The positions of the large pieces are random, and so the distribution curves from different shots show their spikes at different positions.

The patternator and the still photographs both gave mass distribution. The results from the photographs were from single shots, but the patternator results were from multiple shots (typically 30 ice balls per run). The patternator gave statistically mean results, and so the curves were smooth when compared to the results from the still photographs, i.e., the three curves in Fig. 9. However, when the results from these three single shots were averaged, the curve was also fairly smooth. Figure 10 compares the average of the three curves in Fig. 9, with the corresponding patternator results. Good agreement was found, which could be further improved by taking and analyzing more still photographs.

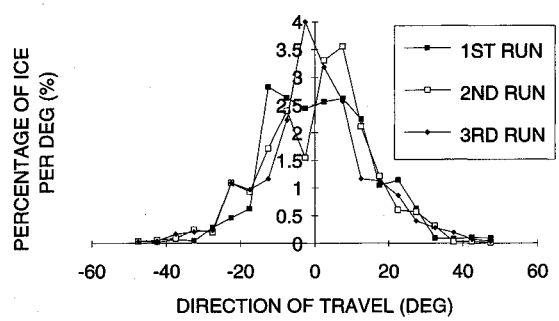

Fig. 9 Postimpact mass distribution. Test case 3: V_0 = 175 m/s, θ = 45 deg, and D_0 = 12.7 mm.

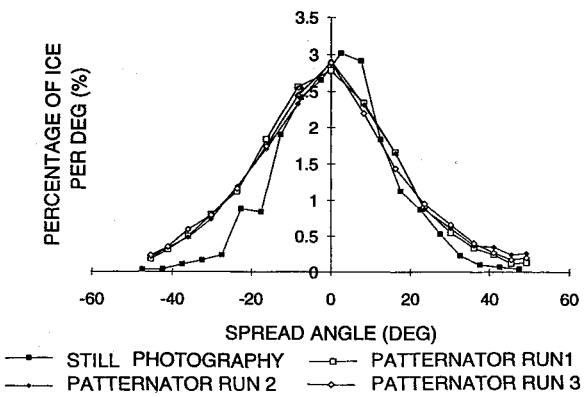

Fig. 10 Comparison of mass distributions obtained with patternator and still photography, test case 3.

Postimpact Particle Velocity

The postimpact velocity was obtained from the double-image photographs (Fig. 4). Although it was easy to identify the two images of a particle by eye, no automatic system was found to measure the distance between the pairs of particles. This time the problem was not only with interpreting the images on the photograph accurately, but also with asking the automatic system to pair the particles. The analysis of the photograph was done manually by projecting the image onto the previously described grid, and measuring the distances between the pairs of particles with a pair of callipers. A typical result is plotted in Fig. 11. As with the size distribution, the mass fraction μ_v, with respect to a certain velocity, was the mass of ice that was traveling at or below the velocity divided by the ice seen on the photograph. Again, the commonly used Rosin–Rammler (Ref. 8) expression was used here,

$$\mu_v = 1 - \exp[-(v/v_{\text{mean}})^{N_v}] \tag{7}$$

in which v_{mean} is the mean particle velocity that is defined as velocity corresponding to 63% of mass fraction, and N_v is the Rosin–Rammler coefficient. As with particle size, $v_{\max}$, v_{mean}, and N_v were shown to vary with approach velocity and approach angle. In establishing the expression of the empirical rules, the postimpact particle velocities and N_v were assumed to be related to both the tangential component of the impact velocity ($V_0 \cos \theta$) and the normal impact energy ($V_0 \sin \theta)^2$. As $\sin^2\theta$ can be easily replaced by $1 - \cos^2\theta$, the expression contains only ($V_0 \cos \theta$) and ($V_0 \cos \theta)^2$. This idea worked well with $v_{\max}$ and N_v, but a linear expression containing only ($V_0 \cos \theta$) gave a better interpretation for the experimental data of

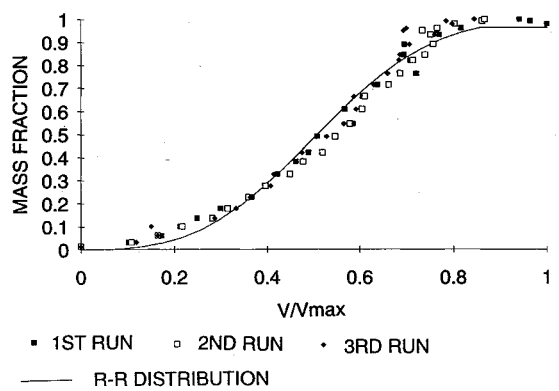

Fig. 11 Postimpact particle velocity distribution, test case 3; Rosin–Rammler parameters: $v_{\max}$ = 169.66 m/s, v_{mean} = 108.7 m/s, and N_v = 2.9.

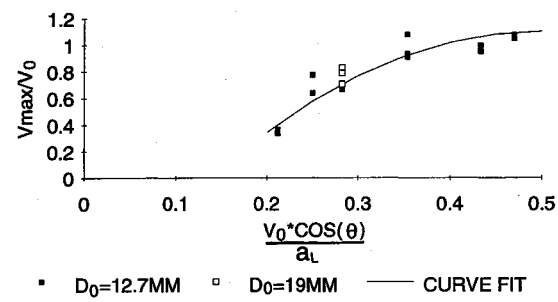

Fig. 12 Curve fit for $v_{\max}$.

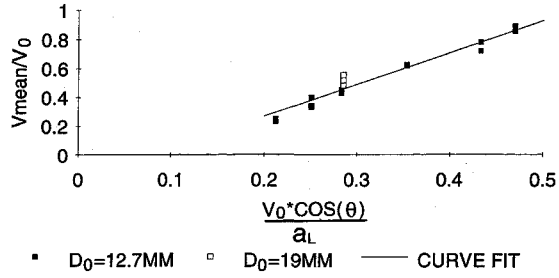

Fig. 13 Curve fit for v_{mean}.

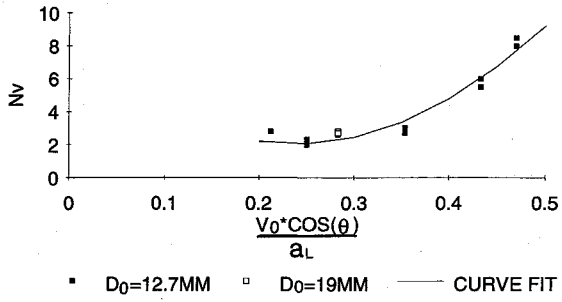

Fig. 14 Curve fit for N_v.

v_{mean}, and the explanation has yet to be found. For the matrix of test cases carried out (Table 1), curve fits using least-square rules were obtained (Figs. 12–14). The expressions describing these curves are

$$v_{max}/V_0 = -1 + 8.4(V_0 \cos \theta/a_L) - 8.4(V_0 \cos \theta/a_L)^2 \quad (8)$$

$$v_{mean}/V_0 = -0.17 + 2.2(V_0 \cos \theta/a_L) \quad (9)$$

$$N_v = 8 - 50(V_0 \cos \theta/a_L) + 105(V_0 \cos \theta/a_L)^2 \quad (10)$$

Like with particle size distribution, Eqs. (8–10) are only valid for the range of experimental data, and a_L should be treated as a constant (a_L = 340 m/s).

Double-imaged photographs used to obtain velocity were not used to get mass distribution. This was because each particle had two images and wiping out one set of images during analysis proved to be impossible. When plotting velocity against mass fraction, a mean mass from the corresponding three single-image photographs was used.

Conclusions

Two experimental techniques were employed to study the basic impact characteristics of ice balls on a flat plate, i.e., patternator, and still photography. The techniques were shown to complement each other and reveal various aspects of the ice impact phenomenon. Basic ice ball impact characteristics in terms of postimpact particle size, postimpact particle velocity, and postimpact mass distribution were obtained. From the experiments, the Rosin–Rammler distribution was found to give good fits to both the particle size and velocity distributions, and the Rosin–Rammler coefficients were shown to be functions of the impact velocity and incidence angle. Based on the experiments, a set of empirical rules was obtained for the Rosin–Rammler coefficients. The coefficients for postimpact particle size were shown to be functions of the normal component of impact velocity, while the postimpact velocity coefficients relied on both the normal and tangential components.

Acknowledgments

This research was sponsored jointly by the Science and Engineering Research Council and Rolls–Royce, plc., England, UK; with additional funding provided by the Civil Aviation Authority.

References

[1]Render, P., Pan, H., Sherwood, M., and Riley, S., "Studies into the Hail Ingestion Characteristics of Turbofan Engines," AIAA Paper 93-2174, June 1993.

[2]Gopalaswamy, N., and Murthy, S. N. B., "Massive Particle Ingestion in Engine Inlet," AIAA Paper 94-0364, Jan. 1994.

[3]Povarov, O., Rastorguev, V., and Bodrov, A., "Interaction of a Drop with Solid Surface," *Power Engineering*, Vol. 24, Pt. 6, 1986, pp. 151–155.

[4]Papadakis, M., Breer, M. D., Craig, N. C., and Bidwell, C. S., "Experimental Water Droplet Impingement Data on Modern Aircraft Surfaces," AIAA Paper 91-0445, Jan. 1991.

[5]Grant, G., and Tabakoff, W., "Erosion Prediction in Turbo-Machinery Resulting from Environmental Solid Particles," *Journal of Aircraft*, Vol. 12, No. 5, 1975, pp. 471–478.

[6]Tabakoff, W., Malak, M. F., and Hamed, A., "Laser Measurement of Solid-Particle Rebound Parameters Impinging on 2024 Aluminium and 6A1-4V Titanium Alloys," *AIAA Journal*, Vol. 25, No. 5, 1987, pp. 721–726.

[7]Tan, S. C., Harris, P. K., and Elder, R. L., "A Unique Test Facility to Measure Particle Restitution and Fragmentation," International Gas Turbine and Aeroengine Congress and Exposition, 94-GT-350, The Hague, The Netherlands, June 1994.

[8]Rosin, P., and Rammler, E., "The Laws Governing the Fitness of Powdered Coal," *Journal of Institute of Fuel*, Vol. 7, Pt. 31, 1933, pp. 29–36.